Analysis of the radiative budget of the Venusian atmosphere based on infrared Net Exchange Rate formalism

Sébastien Lebonnois[1,2], Vincent Eymet[3], Christopher Lee[4], and Jan Vatant d'Ollone[1]

[1]CNRS, UMR 8539, LMD/IPSL, Paris, France, [2]Sorbonne Universités, Pierre et Marie Curie Université, UMR 8539, Paris, France, [3]Meso-Star, Longages, France, [4]Ashima Research, Pasadena, California, USA

Abstract A detailed one-dimensional analysis of the energy balance in Venus atmosphere is proposed in this work, based on the Net Exchange Rate formalism that allows the identification in each altitude region of the dominant energy exchanges controlling the temperature. Well-known parameters that control the temperature profile are the solar flux deposition and the cloud particle distribution. Balance between solar heating and infrared energy exchanges is analyzed for each region: upper atmosphere (from cloud top to 100 km), upper cloud, middle cloud, cloud base, and deep atmosphere (cloud base to surface). The energy accumulated below the clouds is transferred to the cloud base through infrared windows, mostly at 3–4 μm and 5–7 μm. The continuum opacity in these spectral regions is not well known for the hot temperatures and large pressures of Venus's deep atmosphere but strongly affects the temperature profile from cloud base to surface. From cloud base, upward transport of energy goes through convection and short-range radiative exchanges up to the middle cloud where the atmosphere is thin enough in the 20–30 μm window to cool directly to space. Total opacity in this spectral window between the 15 μm CO_2 band and the CO_2 collision-induced absorption has a strong impact on the temperature in the cloud convective layer. Improving our knowledge of the gas opacities in these different windows through new laboratory measurements or ab initio computations, as well as improving the constraints on cloud opacities would help to separate gas and cloud contributions and secure a better understanding of Venus's atmosphere energy balance.

1. Introduction

The thick cloud cover present in the atmosphere of Venus between roughly 47 and 70 km of altitude plays a crucial role in the radiative balance of this system, by reflecting more than 75 % of the incoming solar flux back to space, absorbing half of the remaining flux, and being also optically thick over most of the infrared spectral range. The temperature profile of the atmosphere of Venus is characterized by a very hot troposphere extending from the surface (∼735 K) to roughly 60 km altitude, in the middle clouds. The strong greenhouse effect is provided by the 92 bars of CO_2 that is the main constituent of the atmosphere and by the thick cloud layer.

A recent review of the radiative balance of Venus atmosphere can be found in *Titov et al.* [2007, 2013]. Relevant observations to determine this energy balance are mostly obtained from orbit or from Earth: reflected solar radiation, observed albedo, thermal emission from the cloud top, and thermal emission from the lower atmosphere observed through near-infrared windows. Several probes from the Venera and Pioneer Venus missions provided an additional view from inside, measuring solar and thermal fluxes during descents. The observations from the Venera and Pioneer Venus missions, and the Venus Express mission have allowed development of models to study this energy balance [e.g., *Crisp*, 1986, 1989; *Crisp and Titov*, 1997; *Bullock and Grinspoon*, 2001; *Lee and Richardson*, 2011; *Lee et al.*, 2012]. Temperature, cloud distribution, and properties and abundance of trace gases are all important elements determining this radiative balance.

However, understanding in detail the temperature profile is still a challenge. Above and within the clouds, data sets and modeling have helped to constrain the cloud characteristics [*Zasova et al.*, 1999, 2007; *Haus et al.*, 2013; *Wilquet et al.*, 2009], though their latitudinal variations still need additional investigations [*Wilson et al.*, 2008]. Many uncertainties remain in the opacity of the gas below the clouds, where the pressure and temperature conditions make it difficult to get experimental constraints. The additional difficulty is due to the fact that energy exchanges mainly take place in windows where the opacity of the atmosphere is the smallest, i.e., where it is the most difficult to measure in laboratory [*Wordsworth et al.*, 2010; *Snels et al.*, 2014].

The aim of this study is to use the Net Exchange Rate (NER) formalism of the infrared radiative transfer developed by *Eymet et al.* [2009] to analyze the energy exchanges in the atmosphere and identify the dominant controls on the T profile in a one-dimensional global average approach. This work cannot investigate the impact of latitudinal variations of the cloud structure, an important topic, though this could be the goal for future investigations. In section 2, we describe the infrared model, the solar radiation model used, and the temperature profile computations. The analysis of the radiative budgets is done from the top of the atmosphere (roughly 95–100 km) down to the surface in section 3, detailing the energy balance for each altitude region. These results and the crucial uncertainties identified are discussed in section 4.

2. Methodology

2.1. Infrared Net Exchange Rate Matrix

The infrared radiative transfer we use in this work has been described in *Eymet et al.* [2009]. It is based on the Net Exchange Rate formalism, where the infrared radiative budget of a given atmospheric layer i, ζ_i, is computed as the sum of the radiative net exchanges $\Psi(i, j, \lambda)$ between this layer and all other atmospheric layers j, including the boundaries, i.e., the surface and space:

$$\zeta_i = \sum_\lambda \sum_j \Psi(i, j, \lambda). \tag{1}$$

The wavelength domain considered here is from 1.71 to 250 μm (40–5700 cm^{-1}), divided in 68 narrow bands of variable width [see *Eymet et al.*, 2009, Appendix A].

The individual net exchange rates are computed with

$$\Psi(i, j, \lambda) = \left(B(T_i, \lambda) - B(T_j, \lambda) \right) \xi(i, j, \lambda), \tag{2}$$

where $B(T, \lambda)$ is the Planck function and $\xi(i, j, \lambda)$ is an opticogeometric factor assumed to be temperature independent.

The $\xi(i, j, \lambda)$ matrix is computed with an analytic code on the 50-level vertical grid used in the Laboratoire de Météorologie Dynamique (LMD) Venus general circulation model (GCM) [*Lebonnois et al.*, 2010], with a temperature profile based on a smoothed approximation to the equatorial Venus International Reference Atmosphere (VIRA) model (0–100 km) [*Seiff et al.*, 1985]. Surface pressure is fixed to 92 bars. This analytic computation of the NER matrix (different from the Monte Carlo estimation used in *Eymet et al.* [2009]) is possible when using the hypothesis that the blackbody intensity profile evolves linearly with optical depth within each layer. The angular integration makes use of the exponential integral function $E_n(x) = \int_0^1 \mu^{n-2} \exp(-\frac{x}{\mu}) d\mu$. Details about this computation are given in Appendix A.

To compute the extinction coefficients in each layer and wavelength narrow band, we take into account the following:

1. The atmospheric gaseous composition is similar to the one used in *Eymet et al.* [2009]. This composition mostly comes from the VIRA model [*von Zahn and Moroz*, 1985] and has been used in most radiative transfer works since *Bullock and Grinspoon* [2001] [*Titov et al.*, 2007; *Lee and Richardson*, 2011]. The gas absorption opacities are generated from high-resolution spectral data from HITRAN2008 [*Rothman et al.*, 2009] and HITEMP [*Rothman et al.*, 2010] line-by-line databases with *kspectrum*, a tool developed by Vincent Eymet and available online at http://www.meso-star.com/ en_Products.html. Sub-Lorentzian profiles are taken into account with correcting χ profiles taken from *Pollack et al.* [1993]. Lines are truncated at a distance of 200 cm^{-1}. The spectra are computed in each narrow band for a two-dimensional grid of temperature and pressure relevant to Venus atmospheric conditions and then interpolated along the VIRA pressure-temperature profile on our 50-level vertical grid. A correlated k distribution is then built and approximated with an 8-point Gaussian quadrature.
2. In addition, a continuum can be added to compensate line-by-line approximations due to far-wing line truncation and to include collision-induced absorptions. Several sources of continuum are considered:
   In the near-infrared windows where deep atmospheric radiation is observed from space, the continuum could be constrained from observations. In these windows, we add only these continuum values: 0.7×10^{-9} cm^{-1} amg^{-2} at 1.18 μm [*Bézard et al.*, 2011], 5×10^{-9} cm^{-1} amg^{-2} at 1.74 μm [*de Bergh et al.*, 1995], and 3.5×10^{-8} cm^{-1} amg^{-2} at 2.3 μm [*Marcq et al.*, 2006]. Between these windows, we interpolate

linearly in wave number. We also extrapolate for wavelengths above 2.3 µm, which adds a base continuum of roughly 1×10^{-7} cm^{-1} amg^{-2} at these wavelengths.

CO_2-CO_2 collision-induced absorption (CIA) due to induced dipole moments taken from *Gruszka and Borysow* [1997] in the range [40–250] cm^{-1} ([40–250] µm) are added in all the simulations.

Dimer CO_2-CO_2 collision-induced absorption was also measured in the range [1200–1500] cm^{-1} [*Baranov et al.*, 2004; *Stefani et al.*, 2013] and in the range [2900–3100] cm^{-1} [*Stefani et al.*, 2013], at temperatures up to 450 K and pressures up to 40 bars. We have added this absorption in some simulations, to evaluate the effect. The absorption coefficients in cm^{-1} amg^{-2} are interpolated between the available temperatures and extrapolated up to 740 K.

H_2O CIA continuum can also be estimated from *Clough et al.* [1989], but there is a lot of uncertainty on these values in Venus conditions (high temperature, high pressure). In particular, the formulation of this continuum has been validated only for temperatures below 400 K, while we extrapolate it here to 740 K. We have done simulations without and with this continuum added.

Finally, an arbitrary value of base continuum can be added for wavelengths above 3 µm to mimic the uncertainties that are still present on this continuum and show how they can affect the energy balance. We have done a test with a value of 2×10^{-6} cm^{-1} amg^{-2}.

3. The cloud vertical distribution of particles is different from the one used in *Eymet et al.* [2009]. We use here the cloud model retrieved from VIRTIS/Venus Express and PMV/Venera 15 data by *Haus et al.* [2013, 2014]. The model uses four modes of particles (mode 1: 0.3 µm; mode 2: 1.05 µm; mode 2': 1.4µm; mode 3: 3.65 µm). All parameters for the distribution of these modes are taken from *Haus et al.* [2014] for the low-latitude region. Then using the composition (molar fraction of H_2SO_4 in cloud droplets) and the refraction indexes of H_2SO_4/H_2O mixtures [*Palmer and Williams*, 1975], the efficiency factors, albedos, and asymmetry parameters are computed for each mode, in each spectral narrow band. In a final step, absorption and scattering coefficients are computed using efficiency factors and size distribution parameters, for each particle mode, for each atmospheric layer, in each spectral narrow band.

To illustrate the impact of the cloud distribution, we made a dedicated simulation with a cloud distribution similar to the one used in *Eymet et al.* [2009], taken from *Zasova et al.* [2007] except above 70 km where the number densities (*N*) of modes 1 and 2 are taken from SPICAV and SOIR/Venus Express data analysis [*Wilquet et al.*, 2009]: for mode 1 particles, *N* is approximated to 15 cm^{-3} from 70 to 85 km, then log *N* decreases linearly with altitude down to 1 cm^{-3} at 100 km; for mode 2 particles, log *N* decreases linearly with altitude from 10 cm^{-3} at 70 km down to 0.2 cm^{-3} at 95 km (the impact of this modification of the haze above the main clouds is small).

4. Opacity due to Rayleigh scattering by CO_2 and N_2 is included. As in *Eymet et al.* [2009], it is negligible compared to other opacity sources.

To estimate the sensitivity to wavelength resolution, we computed also the extinction coefficients and $\xi(i, j, \lambda)$ matrix on a much finer spectral grid, using 598 narrow bands, from 0.71 to 250 µm (40–14,000 cm^{-1}). Both distributions of extinction are shown in Figure 1. Figures 1c and 1d allow the visualization of the dominant sources of opacity in each cell. Below 40 µm, the CO_2 absorption bands mostly dominate. In the windows, between these bands, minor compounds and the continuum play a key role, since these windows control most of the energy exchanges in the atmosphere below the clouds, as discussed below. For wavelengths longer than 40 µm, the dominant source of opacity is the CO_2-CO_2 CIA continuum below the clouds. The clouds are clearly dominant above the cloud base over most of the spectrum, apart from the strongest CO_2 absorption bands and far infrared continuum.

The impact of the different possible sources of continuum described above has been evaluated with different simulations, which are summarized in Table 1. The simulation-labeled *dimer* emphasizes the impact of taking into account the opacity of the dimer CO_2-CO_2 CIA in the wave number ranges [1200–1500] cm^{-1} and [2900–3100] cm^{-1}. The simulation-labeled h2o is similar to dimer, but the H_2O CIA continuum is now included. In the simulation-labeled *ctn*, an additional continuum of 2×10^{-6} cm^{-1} amg^{-2} is added to test the sensitivity of the temperature profile to uncertainties on the level of the continuum. Similarly, the simulation-labeled *trnc* illustrates the impact of changing the truncation width for the far-wing profiles. Finally, the simulation-labeled *cld* emphasizes the impact of the cloud distribution: it is similar to the h2o simulation, but the cloud model used is based on *Zasova et al.* [2007] and *Wilquet et al.* [2009] instead of *Haus et al.* [2014], as described above.
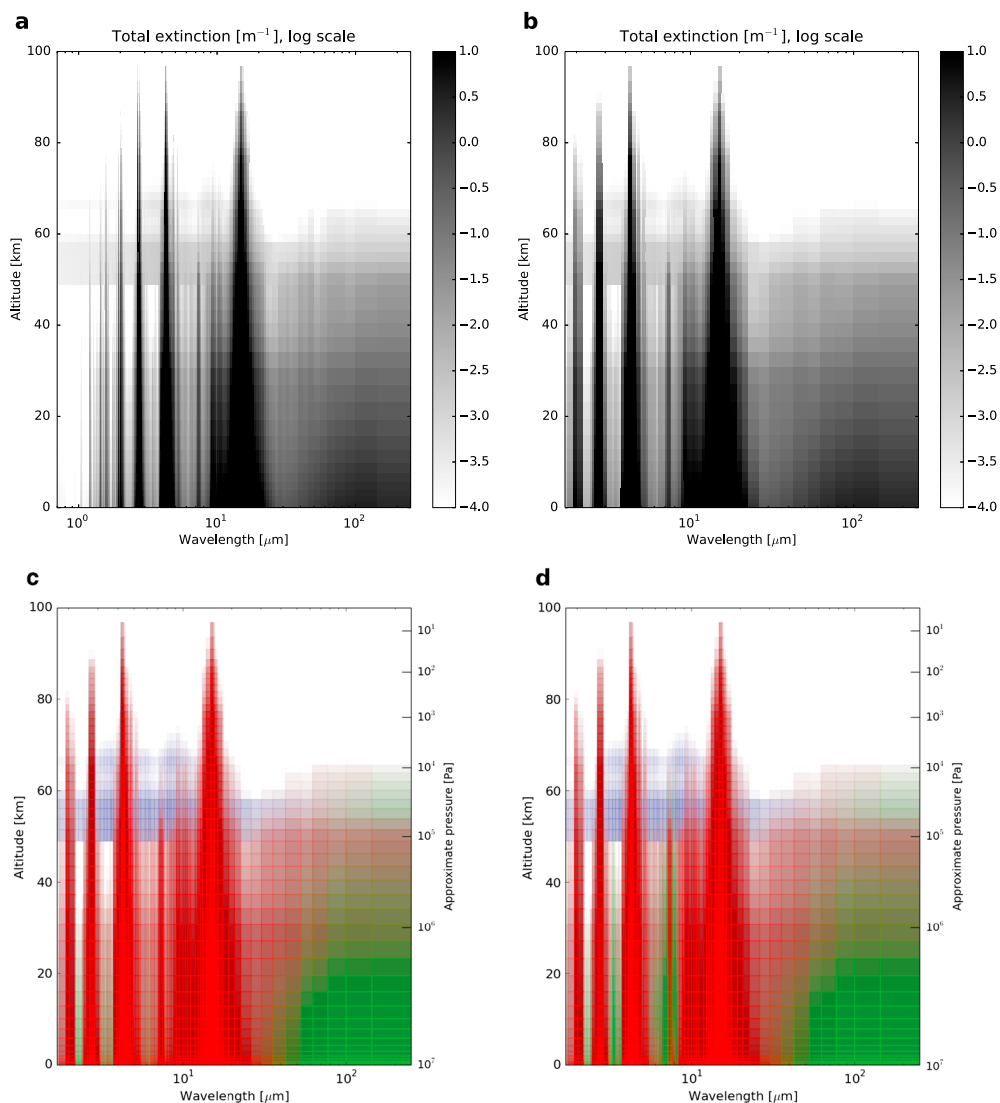
Figure 1. Extinction coefficient distributions in the infrared for our reference computation (*ref*), $\log(k_{tot})$ in m^{-1}, for two different spectral resolutions: (a) 598 narrow bands and (b) 68 narrow bands. Note that the thickness of each layer is always within 1.5 to 4 km in the atmosphere above 5 km altitude (below, it is decreasing toward the surface). (c) Same as Figure 1b but color coded using the relative contribution to the total extinction in each cell as red-green-blue components: red is the fraction due to gas *k* distribution extinction, green is for the total continuum added, and blue is for the cloud extinction. (d) Same as Figure 1c, but for the *h2o* computation (see Table 1). The pressure on the right axis (Figures 1c and 1d) is indicated for reference based on the VIRA temperature profile.

2.2. Solar Flux

As solar flux input, we used for this work the same tables we have been using in our previous Venus GCM studies [*Lebonnois et al.*, 2010], based on *Crisp* [1986]. For the purpose of this work, only a global average is used. The vertical profiles of the net downward solar flux and of the corresponding heating rate are shown in Figure 2, adapted to the 50-level vertical grid of the LMD Venus GCM. Synthesis of observed solar flux was published in the Venus International Reference Atmosphere [*Moroz et al.*, 1985], and the net downward solar flux used here is comparable to the VIRA profile. The dominant feature in this heating rate profile is the strong absorption by the UV absorber in the upper cloud region. The optical properties of this absorber, which has not yet been identified, are listed in Table IV in *Crisp* [1986].

In recent works on radiative transfer for the Venus's atmosphere, both solar and infrared radiations were computed [*Lee and Richardson*, 2011; *Mendonca et al.*, 2015]. This allows in particular to test consistently the impact of varying clouds on both wavelength ranges. In this work, we focus mainly on the infrared computations.

Table 1. Summary of the Characteristics of the Simulations Used in This Work

	ref	dimer	h2o	ctn	trnc	cld	sw
CO_2 dimer CIA		X	X	X	X	X	X
H_2O CIA			X	X	X	X	X
Added continuum[a]	0	0	0	2×10^{-6}	0	0	0
Truncation (cm^{-1})	200	200	200	200	50	200	200
Clouds[b]	H	H	H	H	H	Z+W	H
Solar forcing[c]	C86	C86	C86	C86	C86	C86	LR11

[a] Unit is cm^{-1} amg^{-2}.
[b] H: *Haus et al.* [2013, 2014]; Z+W: *Zasova et al.* [2007] below 70 km and *Wilquet et al.* [2009] above. See text.
[c] C86: solar forcing from *Crisp* [1986]; LR11: solar forcing from *Lee and Richardson* [2011].

However, to illustrate the impact of the solar heating rate profile on the temperature, we also performed a simulation with the globally averaged solar flux profile obtained with the model of *Lee and Richardson* [2011] (simulation-labeled *sw* in Table 1). Compared to *Crisp* [1986], this model uses a different method for the radiative transfer computation, as well as updated values for all the inputs (such as, e.g., the HITRAN 2004 database for gas species spectra). Only the UV absorber optical properties are identical to *Crisp* [1986]. This solar forcing is also plotted in Figure 2.

2.3. Temperature Profile Computations

The computation of the mean vertical temperature profile is done with a one-dimensional version of the LMD Venus GCM [*Lebonnois et al.*, 2010], forced with the globally averaged solar flux. Compared to the physical
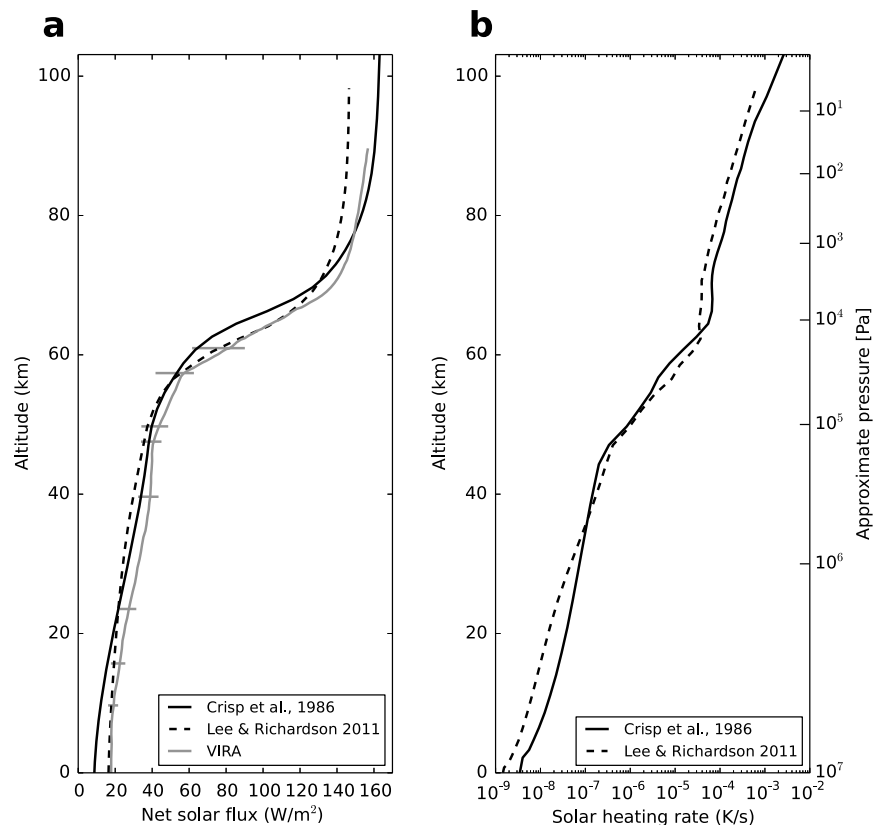

Figure 2. Globally averaged vertical profiles of (a) net downward solar flux and (b) solar heating rate used in the temperature profile simulations: based on *Crisp* [1986] (solid lines) and based on *Lee and Richardson* [2011] (dashed lines). The VIRA profile of the solar flux is shown (in gray) for comparison [*Moroz et al.*, 1985]. The altitude versus pressure profile taken into account here is close to the observed VIRA temperature profile and the pressure on the right axis (Figure 1b) is indicated for reference.
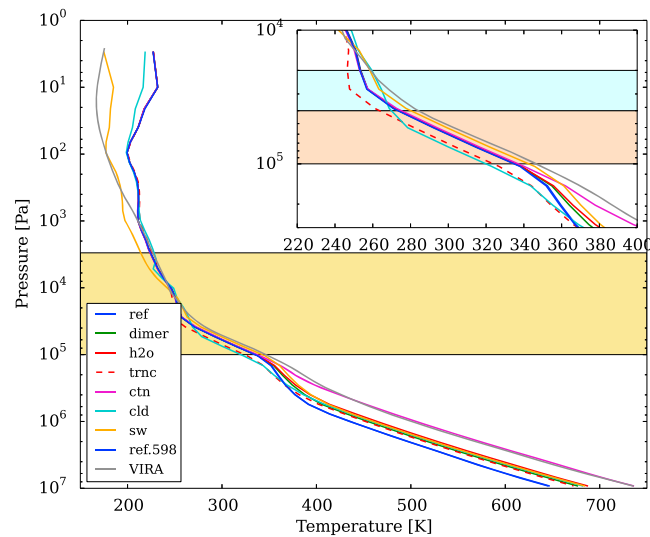
Figure 3. Vertical profiles of temperature obtained with the simulations presented in Table 1. The VIRA profile for low latitudes is shown for comparison [*Seiff et al.*, 1985]. The vertical axis is chosen as pressure since due to the temperature differences in the deep atmosphere, the altitude axis is different for each simulation, making comparisons difficult. (inset) The region around the cloud convective zone is zoomed by a factor of 2 for better visibility. Regions highlighted are discussed in section 3.2.2: clouds (yellow), cloud convective region (pink), and middle-cloud region located between roughly 2×10^4 Pa and the top of the convective layer (light blue).

parametrizations described in *Lebonnois et al.* [2010], the main change concerns the boundary layer scheme. It includes now a "Mellor and Yamada" parametrization [*Mellor and Yamada*, 1982], taken from the Earth version of the LMD GCM and fully described in Appendix B of *Hourdin et al.* [2002]. This new boundary layer scheme affects significantly the temperature profile in the deep atmosphere, close to the surface. The temperature profile is obtained when we reach a steady radiative-convective equilibrium: after 1000 Venus days, the surface temperature is almost stabilized and the outgoing infrared upward flux at the top of the atmosphere balances the incoming solar downward flux within 0.5%.

The vertical profiles of temperature obtained in the simulations are presented in Figure 3. With the different simulations summarized in Table 1, we have tested the sensitivity of the temperature profile to different aspects: the opacity in the range [3–7] µm, the chosen cloud opacity distribution and the solar absorption. For the ref simulation, a run was done with much finer spectral resolution (as mentioned at the end of section 2.1). The results are very close to the corresponding coarser-resolution simulation.

3. Net Exchange Rate Analysis

The $\xi(i, j, \lambda)$ matrix computed for each configuration depends only on the opacity distributions. It can be used to compute the NER matrix $\Psi(i, j, \lambda)$, then the upward, downward, or net infrared fluxes at any level, as well as the infrared radiative budget of a given atmospheric layer. To compute $\Psi(i, j, \lambda)$ for our analysis, the chosen temperature profile may be either the VIRA temperature profile [*Seiff et al.*, 1985] or the radiative-convective equilibrium temperature. In the first case, the fluxes and radiative budgets obtained may be compared to observations to constrain the opacities. In the second case, they are in balance with solar heating rates and convection and may be used to analyze how the temperature profile depends on the different variables involved: opacities and solar heating rates.

3.1. Top-of-Atmosphere Outgoing Radiation

The outgoing flux at the top of the atmosphere (TOA) is computed from the $\xi(i, j, \lambda)$ matrix and the VIRA temperature profile. In Figure 4, this TOA flux is expressed in terms of radiance as a function of wavelength and as a function of wave number, to compare to Figures 1 and 3 of *Titov et al.* [2007]. It is decomposed as a function of wavelength and source layer in Figure 5. This figure clearly illustrates that most of the TOA flux is coming from the cloud region and is therefore controlled by the cloud extinction coefficients, from the cloud top at shorter wavelengths (roughly 5–12 µm) and from the middle cloud around 20–30 µm. Since the cloud model is built from these data, the TOA flux compares well with the observations when computed
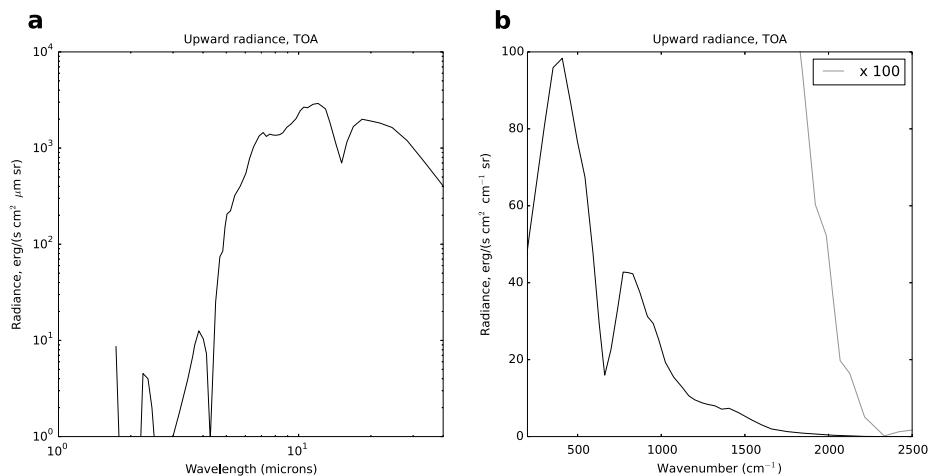
Figure 4. Outgoing flux at the top of the atmosphere computed from the $\xi_{ref}(i,j,\lambda)$ matrix and the VIRA temperature profile, in presentations allowing comparison with observed radiances, Figures 1 and 3 of *Titov et al.* [2007].

with the VIRA temperature profile (though it appears slightly underestimated for the [800 – 900] cm^{-1} (around 12 μm) peak).

In strong CO_2 bands (4.3 and 15 μm), the radiance spectrum depends on the opacity of the gas in the mesosphere, above 80 km altitude, a region where the temperature is more variable than in the clouds. As an example, the 4 to 5 μm region observed by VIRTIS-M/Venus Express is used to retrieve the temperature profile in the 1 – 100 Pa pressure range, roughly 65 to 86 km altitude, in *Grassi et al.* [2008, 2014] and *Haus et al.* [2013, 2014]. In the near-infrared windows (1.74 and 2.3 μm), the TOA flux is coming from the deep atmosphere, and despite using the observed temperatures (VIRA), the flux is underestimated. This may be related to some discrepancy in the opacities used in these windows in our simulations, but also certainly to the impact of scattering in the clouds (see Appendix A).

3.2. Infrared Exchange Budgets

The energy balance in the simulation is shown in Figure 6 for the ref simulation. It is very similar for all simulations. It illustrates that the atmosphere is in radiative equilibrium above the convective layer located in the lower and middle clouds. In the deep atmosphere, convective activity is also present in these simulations.
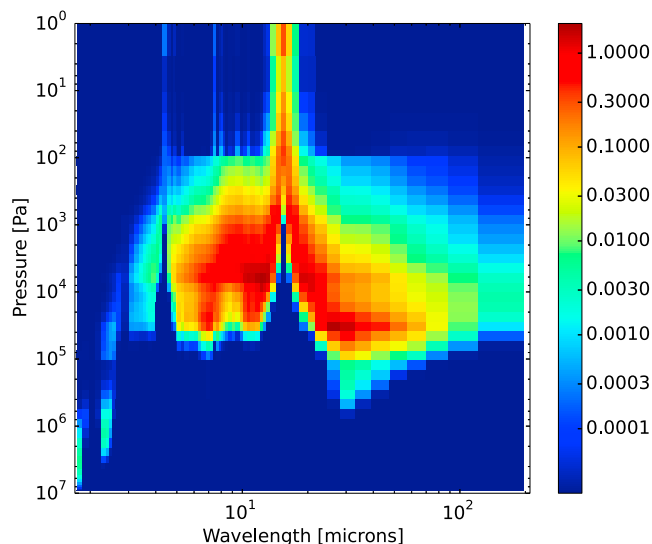

Figure 5. Net exchange rates (in W/m^2/μm, $\xi_{ref}(i,j,\lambda)$ matrix and VIRA temperature profile) between atmospheric layers and space, as a function of wavelength.
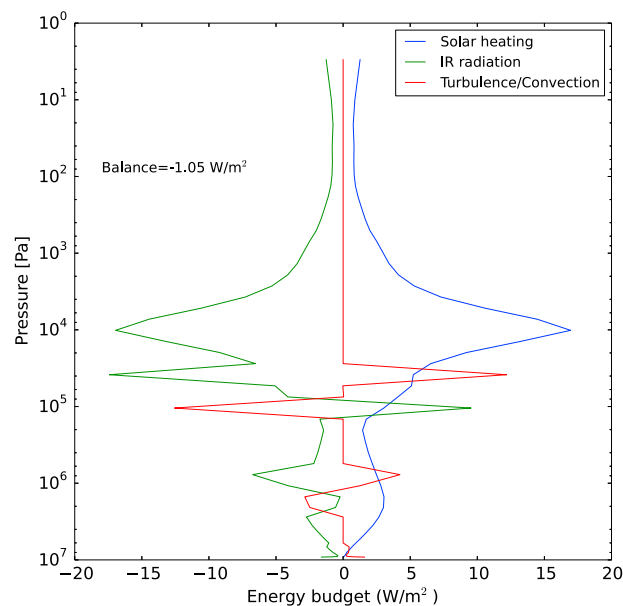
Figure 6. Vertical profile of the heating rate budget (in W/m^2) for simulation ref: solar heating (blue line), infrared radiative budget (green line), and turbulence and convection budget (red line). At the top of the atmosphere, the unbalance between downward solar and upward infrared radiation is indicated: -1.05 W/m^2.

For the different regions of the atmosphere, the infrared net exchange rates are plotted as a function of wavelength in Figure 7. This figure shows the infrared exchanges between one given layer and all other layers, including space, as a function of wavelength. When integrated over wavelength, as plotted in Figure 8, the dominant exchanges can be considered: the short-range exchanges, which are the largest rates, the exchanges with the cloud (mostly base or top), and the cooling to space. Short-range exchanges means that the radiative energy is exchanged between neighbor layers. The typical distance associated with these short-range exchanges is therefore the thickness of a couple of layers (3–7 km).

With the help of these figures, the balance yielding the temperature profile in the different regions of the atmosphere is detailed below.

3.2.1. Upper Atmosphere

The temperature profile obtained above 1×10^3 Pa is largely overestimated (Figure 3). In this region (Figures 7a and 8a), the energy balance is dominated by solar heating, infrared heating from cloud top and levels in-between, and cooling to space. This cooling is mainly provided by the 15 μm CO_2 band. Given that the profile of absorption coefficients for this CO_2 band is well studied for Earth conditions and that here the temperature conditions are close to Earth atmospheric ones, it should be correctly computed. This means that the temperature is then mostly dependent on the amount of heating (no gas opacity uncertainty). Two thirds of this heating comes from solar radiation (0.9 W/m^2 in the level shown in the example, Figures 7a and 8a), the rest (~0.45 W/m^2 in the example) comes from the cloud top and levels in-between, mostly in the wavelength range 6–12 μm which is dominated by cloud opacity (Figure 1c).

The simulation sw done with the alternate solar heating profile from the model of *Lee and Richardson* [2011] (Figure 2) shows that indeed, reducing the solar heating above the clouds reduces the temperature in the upper atmosphere (Figure 3), which helps to get a better agreement with the observed temperature profile.

3.2.2. Clouds

In the upper cloud (between roughly 3×10^3 Pa and 2×10^4 Pa), the temperature is comparable to the VIRA model and to recently observed low-latitude temperatures [e.g., *Tellmann et al.*, 2009; *Grassi et al.*, 2014]. In this region, the energy balance is dominated by the strong solar heating (UV absorber) and infrared cooling to space, with roughly 25% of the cooling done by short-range exchanges. The choice of the cloud model (simulation cld) has only a small impact, because the properties of the upper cloud for the wavelength range where it has a dominant role, namely cooling to space in the 6–12 μm range, are constrained by observed TOA fluxes. As for the atmosphere above, the simulation sw shows that a modification of the solar heating in this region directly affects the temperature.

However, below 2×10^4 Pa, the temperature is slightly colder than the VIRA model (~ 10 K) and becomes very sensitive to the cloud model (see Figure 3, simulations h2o versus cld). Figures 7b and 8b describe the energy balance of the narrow layer between the previous region (upper cloud) and the top of the convective layer that sits in the lower part of the cloud. Here the layer cools to space at wavelengths longer than 15 μm, a spectral region where gaseous opacity is small and dominated by a poorly known continuum, and competes with cloud opacity (Figure 1). In particular, the truncation scheme can affect the far wings of the CO_2 15 μm band and a shorter truncation, such as 50 cm^{-1} instead of 200 cm^{-1} (simulation trnc), affects the continuum opacity in this spectral region, located between the CO_2 15 μm band and the CO_2-CO_2 CIA induced by dipole
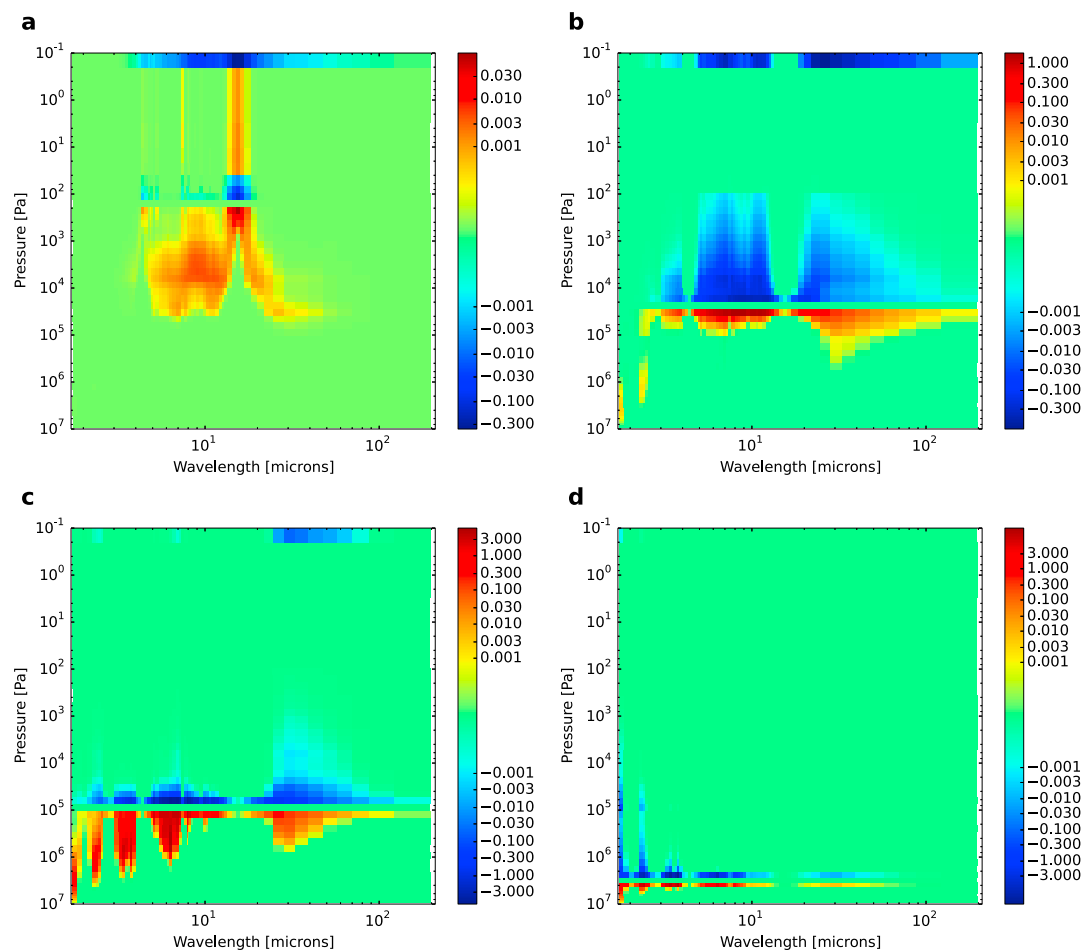
Figure 7. Net exchange rates (in W/m^2/μm, ref simulation) between atmospheric layers and a given layer, as a function of wavelength: (a) at 100 Pa (upper atmosphere), (b) at 3×10^4 Pa (in the cloud, above the convective layer), (c) at 1×10^5 Pa (cloud base), (d) at 3×10^6 Pa (in the deep atmosphere). The topmost layer indicates exchanges with space.

moments. The hypotheses taken in the computation of the gaseous spectrum are then crucial when determining cloud opacities from TOA fluxes in this spectral region, or when computing temperature from a given cloud model (as done here). This sensitivity is illustrated by comparing the temperature profiles (Figure 3) obtained (1) from two different cloud models deduced with different methods and data sets (simulations h2o versus cld) and (2) from gaseous absorption using two different truncations (simulations h2o versus trnc). The two cloud models are not retrieved from the same data sets and differ in retrieval techniques and assumptions. Therefore, they differ in opacity distributions, and the region (in altitude and wavelength) where this is the most critical is the one discussed here. Their difference in cloud opacity for the [15–40] μm range is illustrated in Figure 9.

Using Figures 6 and 8b, the partition of heating sources in this narrow region can be detailed: for the layer shown here, just above the convective layer, solar radiation is roughly 6.6 W/m^2 for a total of 14.1 W/m^2, i.e., ∼47%. The net exchanges within the cloud represent the other 53% and occur in the wavelength range 6–12 μm (Figure 7b), dominated by cloud opacity (Figure 1c). In simulation sw, the heating rate in this region is higher than in the other simulations, and this directly affects the temperature, improving the fit to the VIRA profile.

Between this narrow layer and the cloud base, the energy balance is controlled by convection, and the temperature profile follows the adiabatic lapse rate. The convective region absorbs approximately the same amount of solar heating between simulations sw and the others, the impact on the temperature is similar to the region at the top of the convection (6 K higher). The impact of the cloud model (simulation cld) or of the chosen truncation (simulation trnc) is strong, related to the position of the layer that controls the cooling to space,
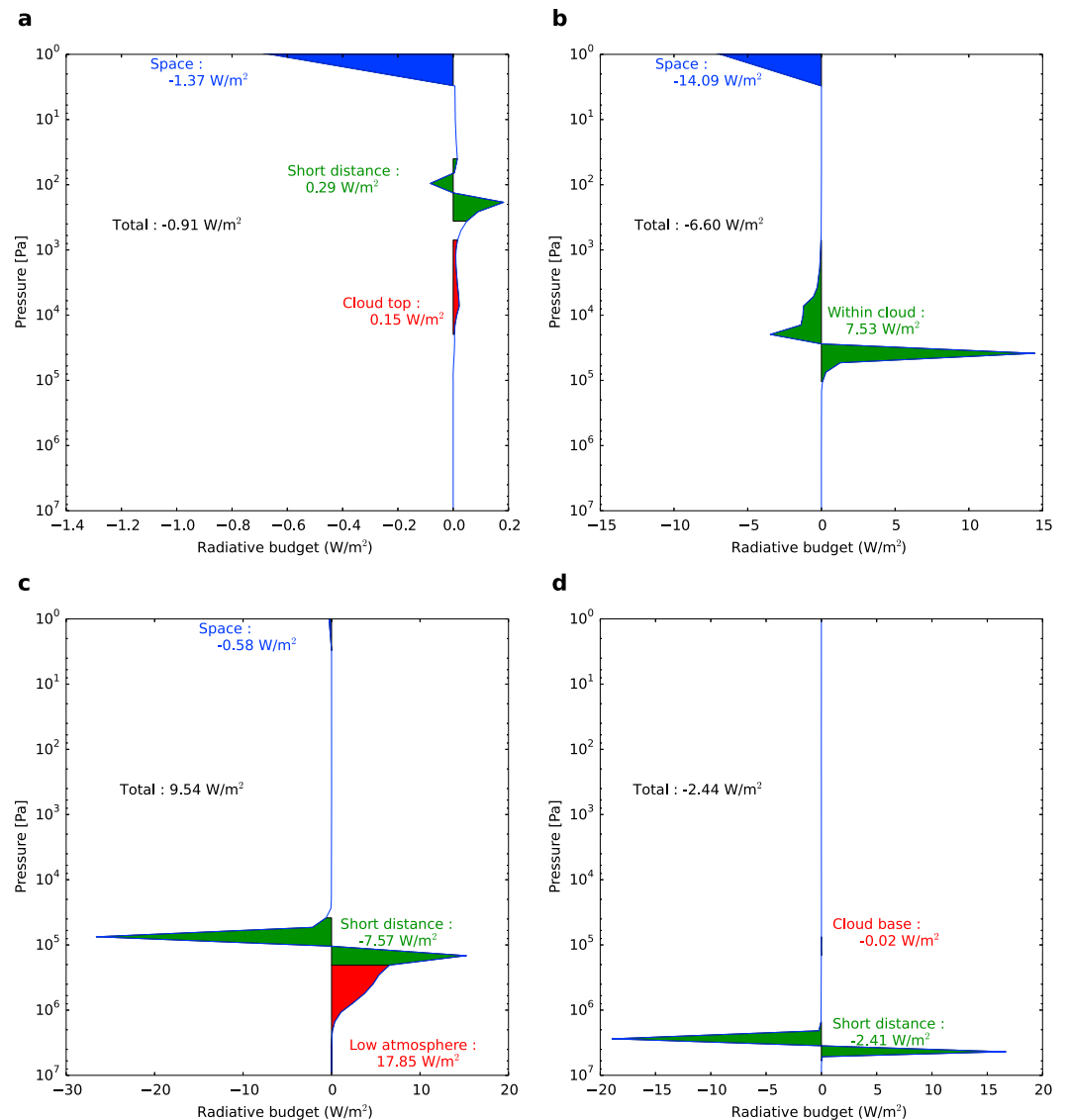
Figure 8. Infrared radiative budgets (in W/m², ref simulation) between atmospheric layers and a given layer: (a) at 100 Pa (upper atmosphere), (b) at 3×10^4 Pa (in the cloud, above the convective layer), (c) at 1×10^5 Pa (cloud base), and (d) at 3×10^6 Pa (in the deep atmosphere). The total budget is detailed between short-distance exchanges, exchanges with clouds, and cooling to space.

discussed above. The balance in this narrow layer at the top of the convective region is therefore crucial to control the temperature at the base of the clouds.

Figures 7c and 8c show that the cloud base is strongly heated by the deep atmosphere (almost 18 W/m², compared to roughly 3 W/m² for the solar heating, as seen in Figure 6), in the spectral windows 3–4 µm and ~5–7 µm, where the opacity is controlled by the continuum (CO_2 and H_2O CIA). Only a fraction (roughly 6%) of this energy is radiated to space, most of it is reaching the top of the convective layer through short-distance infrared radiation and through convection.

3.2.3. Deep Atmosphere and Surface

All the solar radiation reaching below the clouds and depositing energy in the deep atmosphere is transmitted upward in the infrared to the cloud base, mostly through short distance exchanges in the windows between 2 and 7 µm (Figures 7d and 8d).

The distance of the layers below the clouds that can exchange infrared energy with the cloud base through these infrared windows depends strongly on the continuum opacity. The temperature of these layers is
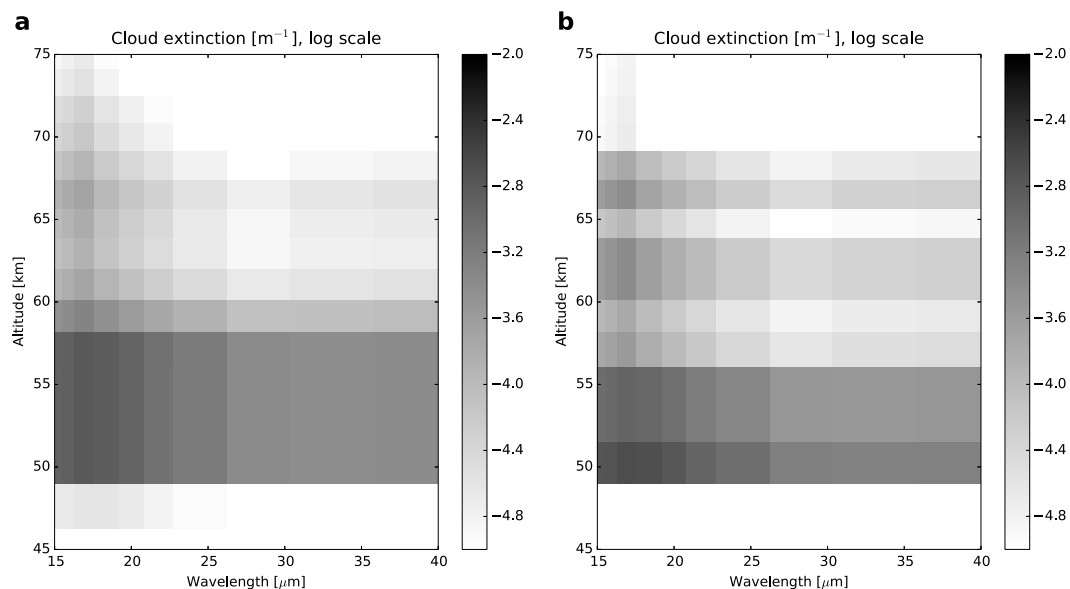
Figure 9. Extinction coefficient distributions in the [15–40] μm range for the two different cloud models used, $\log(k_{cld})$ in m^{-1}: (a) for the *Haus et al.* [2013, 2014] (low latitudes) cloud model and (b) for the *Zasova et al.* [2007] (below 70 km) and *Wilquet et al.* [2009] (above) cloud model.

controlled by the temperature at the cloud base and the total solar heating deposited below the clouds that needs to be balanced. This explains the behavior of the different temperature profiles of the deep atmosphere in Figure 3: the higher opacity in the 3–4 μm and 5–7 μm windows, the closer the layers that can exchange infrared energy with the cloud base, and therefore the higher the overall temperature in the deep atmosphere and at the surface. The impact of the continuum opacity is striking in the temperature differences between the ref, h2o, and ctn simulations (Figure 3).

For simulation sw, the heating rate in this region is smaller than in the other simulations (Figure 2). Because the deep atmosphere balances this input through infrared exchanges to the cloud base, less energy is exchanged between the cloud base and the layers just below (total infrared heating rate received from below is 37 W/m^2 for sw, against 40 W/m^2 for ref or h2o), so the temperature of the deep atmosphere is lower. Despite a cloud base 6 K warmer, the deep atmosphere is 3 K cooler in sw than in h2o.

In the deep atmosphere, the vertical distribution of the solar heating controls whether the short-range infrared exchanges are sufficient to convey upward the solar energy deposited below. The efficiency of this infrared radiative transfer is related to the energy exchanges (computed with the NER matrix in our simulations) and therefore directly linked to opacities in the thinner infrared windows. When the temperature difference needed to transfer all the energy upward gets superadiabatic, convection activates, so that the temperature profile can reach equilibrium. The temperature profile is therefore very close to adiabatic down to the surface. This balance may be different when three-dimensional circulation is taken into account.

4. Discussion

With this work, our goal is to show the respective role of the different sources of uncertainties on the temperature profile: the SW heat profile, the cloud distribution and properties, and the continuum opacity.

Given the properties of the gas in the atmosphere above the cloud top, the temperature in this region is directly controlled by the local solar heating. The exchanges with the cloud top have a significant impact too, but the properties of the cloud top in the spectral range where these exchanges take place (6–12 μm) are constrained by observed TOA flux.

The cloud distribution and properties also control the temperature profile below the cloud top: in the cloud through solar radiation absorption and exchanges with space and in the deep atmosphere through the amount of solar radiation reaching below the clouds. The infrared properties of the clouds are constrained by TOA observations, based on the VIRA temperature profile.

For the surface temperature, this work shows how it depends (1) on the total solar energy deposited below the clouds, (2) on the temperature in the middle cloud (and not the other way around), and (3) on the continuum opacity in the 3–4 μm and 5–7 μm windows.

Points 1 and 2 depend both on the cloud model. The solar energy deposition in and below the clouds depends partly on cloud opacity (together with UV absorber distribution and gases), while temperatures in the cloud depend on solar radiation profile and cloud opacity, mostly in the 6–12 μm spectral range (constrained by TOA flux). The temperature in the middle cloud (point 2) is also strongly dependent on the opacity of the middle and upper cloud and upper atmosphere in the spectral range above 15 μm, through which the middle cloud can cool to space. The opacity in the 3–7 μm windows (point 3) controls the temperatures in the deep atmosphere. When opaque enough, it also slightly affects the temperature at the cloud base and over the whole convective region in the lower and middle cloud. Higher opacity reduces the stable region below the cloud base.

Uncertainties in the gas opacity are crucial in two spectral regions:

1. *[20–30] μm*. This window between the 15 μm band of CO_2 and the CO_2-CO_2 collision-induced absorption due to induced dipole moments is the spectral range in which the middle cloud can cool to space. Therefore, it controls the temperature in the convective region of the clouds. There is no experimental constraints on the gas opacity in Venusian conditions for this window, and the CO_2 absorption in this region is different from one model to the other. Since TOA fluxes constrain the cooling to space of the cloud in this spectral region, uncertainties in the gas opacities will affect also the opacity retrieved for the clouds. Further investigations in this spectral region, combining observed TOA fluxes, observed temperature profiles, and cloud opacity retrievals are needed.

2. *[3–7] μm*. The continuum between the CO_2 bands in this spectral region is controlling the energy exchanges within the deep atmosphere, and between the deep atmosphere and the base of the cloud. Therefore, it controls the surface temperature, for a given cloud base temperature. When using the latest data on CO_2 and H_2O collision-induced absorption in this spectral region, the opacity is not quite enough to get observed surface temperatures when the cloud base temperature is consistent with observations. Additional laboratory measurements of CO_2 absorption in the conditions of the deep atmosphere of Venus (10–100 bars, 500–750 K) where more complex intermolecule interactions may take place are needed to better constrain the energy balance in this region. There is a possibility that additional haze below the cloud may play a significant role here. It is not included in our simulations but may provide additional extinction in this wavelength range between the cloud base and the deep atmosphere.

Improving our knowledge of the gas opacities in these different windows through new laboratory measurements or ab initio computations, as well as improving the constraints on cloud opacities would help to separate gas and cloud contributions and secure a better understanding of Venus atmosphere energy balance.

Appendix A: NER Analytic Computation Tool

The atmosphere is supposed to be divided into *m* homogeneous plane-parallel layers. Within each layer, the blackbody intensity profile is supposed to evolve linearly with optical depth, which roughly corresponds to a linear temperature profile between the interfaces of each layer. When temperatures are provided at layer centers, each one of these initial layers has to be split into two different layers for radiative transfer solving. The quantity of interest is the net exchange rate (NER) between two elements of the atmosphere: element index 0 is the ground, element index *i* (with $1 \leq i \leq m$) is gas layer index *i*, and element $m+1$ is space. The NER is the radiative power emitted by element *i* and absorbed by element *j*, minus the radiative power emitted by *j* and absorbed by *i*. The analytic expressions that are provided below make use of the exponential integral function $E_n(x) = \int_0^1 \mu^{n-2} \exp(-\frac{x}{\mu}) d\mu$.

$\Psi(i, 0, \lambda)$ is the monochromatic NER between gas layer index *i* and a black ground:

$$\Psi(i, 0, \lambda) = 2\pi \left[\left(B(T_1, \lambda) - B(T_g, \lambda) \right) E_3(\tau_{ig}) - \left(B(T_2, \lambda) - B(T_g, \lambda) \right) E_3(\tau_{ig} + \tau_i) \right.$$
$$\left. + \frac{B(T_2, \lambda) - B(T_1, \lambda)}{\tau_i} \left(E_4(\tau_{ig}) - E_4(\tau_{ig} + \tau_i) \right) \right] \tag{A1}$$

with T_1 and T_2 are temperatures at the bottom and at the top of layer *i* (assuming a linear blackbody profile between the bottom and top interfaces of the layer), T_g is the temperature of the ground, τ_i is the optical

depth of layer i, and τ_{ig} is the optical thickness between the ground and the bottom interface of layer i. $B(T, \lambda)$ is the monochromatic blackbody intensity (Planck function) in W/m²/sr/μm.

$\Psi(i, m + 1, \lambda)$ is the monochromatic NER between gas layer i and space:

$$\Psi(i, m + 1, \lambda) = 2\pi \left[\left(B(T_2, \lambda) - B(T_s, \lambda)\right) E_3(\tau_{is}) - \left(B(T_1, \lambda) - B(T_s, \lambda)\right) E_3(\tau_{is} + \tau_i) \right.$$
$$\left. - \frac{B(T_2, \lambda) - B(T_1, \lambda)}{\tau_i} \left(E_4(\tau_{is}) - E_4(\tau_{is} + \tau_i)\right) \right] \tag{A2}$$

with T_s is the temperature of space (if not set at 0 K) and τ_{is} is the optical thickness between the top interface of layer i and space.

$\Psi(i, j, \lambda)$ is the monochromatic NER between layers index i and j (with $i < j$ and $j \leq m$):

$$\Psi(i, j, \lambda) = 2\pi \left[\left(B(T_2, \lambda) - B(T_3, \lambda)\right) E_3(\tau_{ij}) + \left(B(T_3, \lambda) - B(T_1, \lambda)\right) E_3(\tau_{ij} + \tau_i) \right.$$
$$+ \left(B(T_4, \lambda) - B(T_2, \lambda)\right) E_3(\tau_{ij} + \tau_j) + \left(B(T_1, \lambda) - B(T_4, \lambda)\right) E_3(\tau_{ij} + \tau_i + \tau_j)$$
$$+ \left(\frac{B(T_2, \lambda) - B(T_1, \lambda)}{\tau_i} + \frac{B(T_4, \lambda) - B(T_3, \lambda)}{\tau_j} \right) \tag{A3}$$
$$\left. \left(\left(E_4(\tau_{ij} + \tau_i) + E_4(\tau_{ij} + \tau_j) - E_4(\tau_{ij}) - E_4(\tau_{ij} + \tau_i + \tau_j)\right)\right) \right]$$

with T_3 and T_4 are the temperatures at the bottom and top of layer j, τ_j is the optical thickness of layer j, and τ_{ij} is the optical thickness between the top interface of layer i and the bottom interface of layer j.

Finally, $\Psi(0, m + 1, \lambda)$ is the NER between the ground and space:

$$\Psi(0, m + 1, \lambda) = 2\pi \left(B(T_g, \lambda) - B(T_s, \lambda)\right) E_3(\tau_{gs}) \tag{A4}$$

with τ_{gs} is the optical thickness between the ground and space.

Similar expressions can be found for a reflecting ground (both specular and diffuse) but are not provided here.

Then the monochromatic radiative budget $\zeta_i(\lambda)$, average over layer i, is provided by

$$\zeta_i(\lambda) = \sum_{j=0}^{m+1} \Psi(i, j, \lambda) \tag{A5}$$

The monochromatic net flux (upward to downward) at a given interface index k (interface 0 is the ground, interface 1 is at the top of layer 1, interface k is at the top of layer index k) $\Phi_k(\lambda)$ is provided by

$$\Phi_k(\lambda) = \sum_{i=0}^{k} \sum_{j=k+1}^{m+1} \Psi(i, j, \lambda) \tag{A6}$$

Then, all quantities can be spectrally integrated. Since we used a correlated k spectral model, all radiative quantities are computed for each quadrature point, in each spectral interval. The optical depth between two interfaces τ_i is obtained from absorption coefficients k_1 and k_2 (at the bottom and top interfaces of layer i, of respective altitudes z_1 and z_2) assuming the absorption coefficient evolves as the local gas density, i.e., as a decreasing exponential of altitude:

$$\tau_i = (z_2 - z_1) \frac{k_1 - k_2}{\log(\frac{k_1}{k_2})} \tag{A7}$$

Absorption coefficients at each interface have to take into account the presence of a gas mixture and potential clouds:

$$k = k(\text{gas}) + k(\text{clouds}) \tag{A8}$$

Scattering. The KARINE code that was used in *Eymet et al.* [2009] was a Monte Carlo code that took scattering completely into account. This is not the case in the analytic formulation used here, used because of the huge gain in computation speed. Whenever scattering has to be taken into account, the absorption coefficients that

should be taken into account in equation (A7) must account for absorption and scattering properties of the participating medium, where the asymmetry parameter g of the phase function is taken into consideration:

$$k(\text{clouds}) = k_{\text{abs}}(\text{clouds}) + (1 - g)k_{\text{sca}}(\text{clouds}) \qquad (A9)$$

We compared the vertical profiles of the radiative budget computed with both codes in the same conditions. Except at the edges of the clouds, the differences are barely noticeable and within the Monte Carlo error bars. This can be understood because absorption in the clouds is strong enough at most wavelengths to attenuate quickly the scattered rays.

However, for the near-infrared windows, this approximation is not valid and this affects the TOA signal in these windows. Since it is negligible in the radiative budget, this approximation is not a problem for the present work.

References

Baranov, Y. I., W. J. Lafferty, and G. T. Fraser (2004), Infrared spectrum of the continuum and dimer absorption in the vicinity of the O_2 vibrational fundamental in O_2/CO_2 mixtures, *J. Mol. Spectrosc.*, *228*, 432–440, doi:10.1016/j.jms.2004.04.010.

Bézard, B., A. Fedorova, J. -L. Bertaux, A. Rodin, and O. Korablev (2011), The 1.10- and 1.18-μm nightside windows of Venus observed by SPICAV-IR aboard Venus Express, *Icarus*, *216*, 173–183, doi:10.1016/j.icarus.2011.08.025.

Bullock, M. A., and D. H. Grinspoon (2001), The recent evolution of climate on Venus, *Icarus*, *150*, 19–37, doi:10.1006/icar.2000.6570.

Clough, S. A., F. X. Kneizys, and R. W. Davies (1989), Line shape and the water vapor continuum, *Atmos. Res.*, *23*, 229–241, doi:10.1016/0169-8095(89)90020-3.

Crisp, D. (1986), Radiative forcing of the Venus mesosphere. I—Solar fluxes and heating rates, *Icarus*, *67*, 484–514.

Crisp, D. (1989), Radiative forcing of the Venus mesosphere. II—Thermal fluxes, cooling rates, and radiative equilibrium temperatures, *Icarus*, *77*, 391–413.

Crisp, D., and D. Titov (1997), The thermal balance of the Venus atmosphere, in *Venus II, Geology, Geophysics, Atmosphere, and Solar Wind Environnement*, edited by D. Crisp and D. Titov, pp. 353–384, Univ. of Arizona Press, Tucson, Ariz.

de Bergh, C., B. Bezard, D. Crisp, J. P. Maillard, T. Owen, J. Pollack, and D. Grinspoon (1995), Water in the deep atmosphere of Venus from high-resolution spectra of the night side, *Adv. Space Res.*, *15*, 79–88, doi:10.1016/0273-1177(94)00067-B.

Eymet, V., R. Fournier, J. -L. Dufresne, S. Lebonnois, F. Hourdin, and M. A. Bullock (2009), Net-exchange parameterization of the thermal infrared radiative transfer in Venus' atmosphere, *J. Geophys. Res.*, *114*, E11008, doi:10.1029/2008JE003276.

Grassi, D., P. Drossart, G. Piccioni, N. I. Ignatiev, L. V. Zasova, A. Adriani, M. L. Moriconi, P. Irwin, A. Negrão, and A. Migliorini (2008), Retrieval of air temperature profiles in the Venusian mesosphere from VIRTIS-M data: Description and validation of algorithms, *J. Geophys. Res.*, *113*, E00B09, doi:10.1029/2008JE003075.

Grassi, D., R. Politi, N. I. Ignatiev, C. Plainaki, S. Lebonnois, P. Wolkenberg, L. Monatbone, A. Migliorini, G. Piccioni, and P. Drossart (2014), The Venus nighttime atmosphere as observed by VIRTIS-M instrument. Average fields from the complete infrared data set, *J. Geophys. Res. Planets*, *119*, 837–849, doi:10.1002/2013JE004586.

Gruszka, M., and A. Borysow (1997), Roto-translational collision-induced absorption of CO_2 for the atmosphere of Venus at frequencies from 0 to 250 cm^{-1}, at temperatures from 200 to 800 K, *Icarus*, *129*, 172–177, doi:10.1006/icar.1997.5773.

Haus, R., D. Kappel, and G. Arnold (2013), Self-consistent retrieval of temperature profiles and cloud structure in the northern hemisphere of Venus using VIRTIS/VEX and PMV VENERA-15 radiation measurements, *Planet. Space Sci.*, *89*, 77–101, doi:10.1016/j.pss.2013.09.020.

Haus, R., D. Kappel, and G. Arnold (2014), Atmospheric thermal structure and cloud features in the Southern Hemisphere of Venus as retrieved from VIRTIS/VEX radiation measurements, *Icarus*, *232*, 232–248, doi:10.1016/j.icarus.2014.01.020.

Hourdin, F., F. Couvreux, and L. Menut (2002), Parameterization of the dry convective boundary layer based on a mass flux representation of thermals, *J. Atmos. Sci.*, *59*, 1105–1123.

Lebonnois, S., F. Hourdin, V. Eymet, A. Crespin, R. Fournier, and F. Forget (2010), Superrotation of Venus' atmosphere analysed with a full general circulation model, *J. Geophys. Res.*, *115*, E06006, doi:10.1029/2009JE003458.

Lee, C., and M. I. Richardson (2011), A discrete ordinate, multiple scattering, radiative transfer model of the Venus atmosphere from 0.1 to 260 μm, *J. Atmos. Sci.*, *68*, 1323–1339, doi:10.1175/2011JAS3703.1.

Lee, Y. J., D. V. Titov, S. Tellmann, A. Piccialli, N. Ignatiev, M. Pätzold, B. Häusler, G. Piccioni, and P. Drossart (2012), Vertical structure of the Venus cloud top from the VeRa and VIRTIS observations onboard Venus Express, *217*(Icarus), 599–609, doi:10.1016/j.icarus.2011.07.001.

Marcq, E., T. Encrenaz, B. Bézard, and M. Birlan (2006), Remote sensing of Venus' lower atmosphere from ground-based IR spectroscopy: Latitudinal and vertical distribution of minor species, *Planet. Space Sci.*, *54*, 1360–1370.

Mellor, G. L., and T. Yamada (1982), Development of a turbulent closure model for geophysical fluid problems, *Rev. Geophys.*, *20*, 851–875.

Mendonca, J. M., P. L. Read, C. F. Wilson, and C. Lee (2015), A new fast and flexible radiative transfer method for Venus general circulation models, *Planet. Space Sci.*, *105*, 80–93, doi:10.1016/j.pss.2014.11.008.

Moroz, V. I., A. P. Ekonomov, B. E. Moshkin, H. E. Revercomb, L. A. Sromovsky, and J. T. Schofield (1985), Solar and thermal radiation in the Venus atmosphere, *Adv. Space Res.*, *5*, 197–232.

Palmer, K., and D. Williams (1975), Optical constants of sulfuric acid: Application to the clouds of Venus, *Appl. Opt.*, *14*, 208–219.

Pollack, J. B., et al. (1993), Near-infrared light from Venus' nightside — A spectroscopic analysis, *Icarus*, *103*, 1–42.

Rothman, L. S., et al. (2009), The HITRAN 2008 molecular spectroscopic database, *J. Quant. Spectrosc. Radiat. Transfer*, *110*, 533–572, doi:10.1016/j.jqsrt.2009.02.013.

Rothman, L. S., I. E. Gordon, R. J. Barber, H. Dothe, R. R. Gamache, A. Goldman, V. I. Perevalov, S. A. Tashkun, and J. Tennyson (2010), HITEMP, the high-temperature molecular spectroscopic database, *J. Quant. Spectrosc. Radiat. Transfer*, *111*, 2139–2150, doi:10.1016/j.jqsrt.2010.05.001.

Seiff, A., et al. (1985), Model of the structure of the atmosphere of Venus from surface to 100 km altitude, *Adv. Space Res.*, *5*(11), 3–58.

Snels, M., S. Stefani, D. Grassi, G. Piccioni, and A. Adriani (2014), Carbon dioxide opacity of the Venus' atmosphere, *Planet. Space Sci.*, *103*, 347–354, doi:10.1016/j.pss.2014.08.002.

Stefani, S., G. Piccioni, M. Snels, D. Grassi, and A. Adriani (2013), Experimental CO_2 absorption coefficients at high pressure and high temperature, *J. Quant. Spectrosc. Radiat. Transfer*, *117*, 21–28, doi:10.1016/j.jqsrt.2012.11.019.

Tellmann, S., M. Pätzold, B. Hausler, M. K. Bird, and G. L. Tyler (2009), Structure of the Venus neutral atmosphere as observed by the radio science experiment VeRa on Venus Express, *J. Geophys. Res.*, *114*, E00B36, doi:10.1029/2008JE003204.

Titov, D. V., M. A. Bullock, D. Crisp, N. O. Renno, F. W. Taylor, and L. V. Zasova (2007), Radiation in the atmosphere of Venus, in *Exploring Venus as a Terrestrial Planet, Geophys. Monogr. Ser.*, vol. 176, edited by D. V. Titov et al., pp. 121–138, AGU, Washington, D. C.

Titov, D. V., G. Piccioni, P. Drossart, and W. J. Markiewicz (2013), Radiative energy balance in the Venus atmosphere, in *Towards Understanding the Climate of Venus: Application of Terrestrial Models to Our Sister Planet, ISSI Sci. Rep. Ser.*, vol. 11, edited by L. Bengtsson et al., pp. 23–53, Springer, Netherlands.

von Zahn, U., and V. Moroz (1985), Composition of the Venus atmosphere below 100 km altitude, *Adv. Space. Res.*, *5*, 173–195.

Wilquet, V., A. Fedorova, F. Montmessin, R. Drummond, A. Mahieux, A. C. Vandaele, E. Villard, O. Korablev, and J. -L. Bertaux (2009), Preliminary characterization of the upper haze by SPICAV/SOIR solar occultation in UV to mid-IR onboard Venus Express, *J. Geophys. Res.*, *114*, E00B42, doi:10.1029/2008JE003186.

Wilson, C. F., S. Guerlet, P. G. Irwin, C. C. Tsang, F. W. Taylor, R. W. Carlson, P. Drossart, and G. Piccioni (2008), Evidence for anomalous cloud particles at the poles of Venus, *J. Geophys. Res.*, *113*, E00B13, doi:10.1029/2008JE003108.

Wordsworth, R. D., F. Forget, and V. Eymet (2010), Infrared collision-induced and far-line absorption in dense CO_2 atmospheres, *Icarus*, *210*, 992–997, doi:10.1016/j.icarus.2010.06.010.

Zasova, L. V., I. A. Khatountsev, V. I. Moroz, and N. I. Ignatiev (1999), Structure of the Venus middle atmosphere: Venera 15 Fourier spectrometry data revisited, *Adv. Space Res.*, *23*(9), 1559–1568.

Zasova, L. V., N. I. Ignatiev, I. A. Khatuntsev, and V. Linkin (2007), Structure of the Venus atmosphere, *Planet. Space Sci.*, *55*, 1712–1728, doi:10.1016/j.pss.2007.01.011.